

Photorefractive parameters of lithium niobate crystals from photoinduced light scattering

M. Goulkov

Institute of Physics, Science Ave 46, 03650, Kiev-39, Ukraine

M. Imlau

Department of Physics, University of Osnabrück, Barbara Strasse 7, D-49069 Osnabrück, Germany

Th. Woike

Institute of Mineralogy, University of Cologne, Zùlpicher Strasse 49b, D-50674 Cologne, Germany

(Received 9 April 2008; revised manuscript received 8 May 2008; published 13 June 2008)

Photoinduced light scattering (PILS) in nominally undoped LiNbO_3 with the mixed photovoltaic and diffusion charge transports is studied theoretically and experimentally. All parameters describing the holographic behavior of LiNbO_3 are received from the angular distribution of the scattering intensity: gain factor Γ , diffusion field E_D , photovoltaic field E_{pv} , and frequency detuning $\Omega\tau_{di}$. The technical advantage of this PILS method is the low requirement of mechanical stability.

DOI: [10.1103/PhysRevB.77.235110](https://doi.org/10.1103/PhysRevB.77.235110)

PACS number(s): 42.65.Hw, 42.70.Nq, 78.20.Jq

I. INTRODUCTION

Propagation of laser beams in photorefractive crystals is always accompanied by the effect of the photoinduced light scattering (PILS).¹⁻³ PILS is the result of amplification of the scattered light due to the nonlinear coupling with the pump beam on noisy photorefractive index gratings. Particularly, a rich variety of scattering processes is reported in LiNbO_3 , a promising nonlinear optic material. PILS can be a serious drawback of the crystal because it strongly reduces the signal-to-noise ratio in different applications.^{4,5} At the same time, it is shown that the PILS phenomenon can be alternatively implemented in different optical schemes of image amplification and processing.⁶⁻⁸ Also, since PILS is the characteristic fingerprint of light amplification processes and strongly depends on crystal properties, it can be a very useful tool for a comprehensive determination and analysis of various characteristics of photorefractive crystals.⁹⁻¹² All of this makes a detailed theoretical and experimental study of the scattering, an important task nowadays.

One of the most fascinating PILS manifestations in LiNbO_3 is the wide-angle polarization-isotropic scattering induced by a single pump beam of the extraordinary polarization. This scattering is particularly efficient in iron and copper doped samples characterized by the strong photovoltaic effect. The physics of this scattering process is an ongoing discussion. The photorefractive response driven by the photovoltaic charge transport is local and does not allow the stationary energy exchange between recording waves as it takes place in $\text{Sr}_{0.61}\text{Ba}_{0.39}\text{Nb}_2\text{O}_6$ (SBN) or in BaTiO_3 . Here, the diffusion charge transport provides a purely nonlocal response and results in the scattering amplification in the direction opposite to the polar c axis of the crystal.^{1,13} Surprisingly, the scattering observed in LiNbO_3 is very efficient and it shows different spatial properties: The scattering pattern consists of two lobes in $\pm c$ directions. Only recently, the model of two-wave mixing (2WM) on moving gratings recorded at the presence of a low-frequency noise was proposed, which is able to explain the amplification of the scattering in photorefractive crystals with dominating photovoltaic response.²

In the present work, the detailed theoretical and experimental study of the wide-angle polarization-isotropic PILS is carried out for undoped lithium niobate. The scattering model is considered for the case of diffusion having a magnitude comparable with the photovoltaic effect. Properties of initial and stationary scattering are measured in a wide angular range. The new method of determination of the angular dependence of the coupling coefficient as well as of diffusion and photovoltaic fields from the scattering profiles is developed. A good agreement of the experimental and theoretical results is demonstrated.

II. MODEL OF WIDE-ANGLE POLARIZATION-ISOTROPIC PHOTOINDUCED LIGHT SCATTERING IN LiNbO_3

The wide-angle polarization-isotropic scattering is the result of nonlinear amplification of coherent optical noise at the expense of the pump beam via 2WM on elementary noisy gratings of the index of refraction. The coherent optical noise is the initial scattering that emerges on optical inhomogeneities of the crystal and interferes with the pump beam. It has the same polarization as the incident light and propagates at different angles θ_s^n in the crystal. A multitude of single gratings $\mathbf{K}=\mathbf{k}_p-\mathbf{k}_s$ is recorded by pairs of pump (\mathbf{k}_p) and scattering (\mathbf{k}_s) waves via the photorefractive effect.¹⁴ Successive processes of the photoexcitation of electrons (dominating electric carriers) in bright interference fringes and their posterior migration and trapping in dark interference fringes yield the space-charge field, which spatially modulates the index of refraction via the linear electro-optic effect. The diffusion and the photovoltaic effect are considered as main charge transports in undoped LiNbO_3 . The largest electro-optic coefficient r_{33} determines the development of the strongest scattering in the plane of incidence.

An effective amplification of the scattering via 2WM requires a nonzero mismatch between interference and refractive index patterns. The bidirectional scattering pattern is elongated in $\pm c$ directions, as reported for LiNbO_3 ,¹⁵⁻¹⁷ that

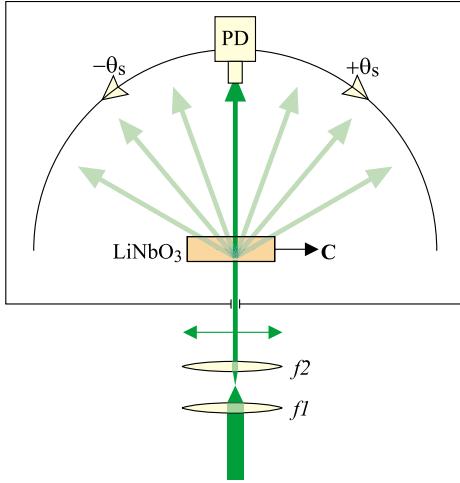


FIG. 1. (Color online) Experimental setup for the observation of the wide-angle polarization-isotropic PILS in LiNbO₃ crystal. Coherent illumination is performed by a single beam of extraordinary polarization ($\lambda=532$ nm) passing the lenses $f1$ and $f2$. The c axis of the crystal is in the plane of incidence. The scattering is monitored by a photodiode rotating around the crystal, closed in the black box.

assumes the same grating shift in $\pm c$ directions. In the limit of an elastic scattering ($\omega_s = \omega_p$), the local photovoltaic charge transport provides a recording of unshifted gratings, which does not contribute to the stationary scattering amplification. Diffusion-driven gratings possess a $\pi/2$ phase shift, and 2WM on these gratings causes the amplification of the light scattered only in the $-c$ direction. Therefore, the one-directional scattering pattern is expected, which contradicts to the experimental observations. In Ref. 2 this problem is solved by taking into account small frequency detuning $\Omega = \omega_p - \omega_s$ between pump and scattering waves. A nonzero frequency difference causes a permanent mismatch between moving interference patterns and recorded index gratings. This additional shift reduces the diffusion contribution to the scattering amplification but enables a considerable enhancement of the scattering via the photovoltaic response. Frequency detuning in scattered light is experimentally detected in different photorefractive materials.^{2,17,18} The nature of such detuning is not yet well studied.

The analysis is based on the simplified 2WM solution derived in the undepleted pump approximation. The stationary intensity of the scattering amplified on the grating \mathbf{K} is

$$I_s = I_{so}^{\Omega} \exp(\Gamma l_{\text{eff}}), \quad (1)$$

where I_{so}^{Ω} is the initial scattering intensity, which properties are governed by a low-frequency noise, Γ is the coupling coefficient (or gain factor), and l_{eff} is the effective coupling length. We assume normal incidence of the single laser beam of extraordinary polarization to the c axis of the crystal in the following, as shown in Fig. 1. Also, only scattering waves propagating in the plane of incidence are considered.

A. Coupling coefficient $\Gamma(\theta_s)$

The coefficient Γ in Eq. (1) describes the efficiency of the pump-scattering coupling at the presence of a low-frequency

noise in the photorefractive response resulting in small frequency detuning Ω between interacting waves. This is equivalent to 2WM on a single grating moving in space with a speed $v = 2\pi\Omega K^{-1}$. We assume that the main contribution to the frequency detuning is caused by temporal fluctuations in the photoelectric processes of the formation of the space-charge field and the electro-optic modulation of the refractive index.

Taking into account the normal incidence of the pump beam and the off-axis propagation of scattering components, Γ can be written as^{14,19}

$$\Gamma = \text{Re} \left\{ \frac{i4\pi\Delta n}{\lambda \sqrt{\cos^2 \theta_s^{\text{in}} (1 + i\Omega\tau_{\text{di}})}} \right\}, \quad (2)$$

where θ_s^{in} is the scattering angle measured from the propagation direction of the pump beam, τ_{di} is the Maxwell relaxation time, and $E_{pv}(\theta_s^{\text{in}})$ is the grating amplitude dependent on the linear electro-optic coefficients $l_{\text{eff}}(\theta_s^{\text{in}})$ and $I_{so}^{\Omega}(\theta_s^{\text{in}})$, and the refractive indices n_e and n_o ,

$$\Delta n = \frac{E_{\text{sc}}}{2m} \left[n_e^3 r_{33} \cos \theta_s^{\text{in}} \cos \left(\frac{\theta_s^{\text{in}}}{2} \right) + n_e n_o^2 r_{42} \sin \theta_s^{\text{in}} \sin \left(\frac{\theta_s^{\text{in}}}{2} \right) \right], \quad (3)$$

where m is the modulation depth. E_{sc} is the amplitude of the space-charge field induced in the crystal,

$$E_{\text{sc}} = im \frac{-E_D + iE_{pv}}{1 + \frac{-E_D + iE_{pv}}{E_q}}, \quad (4)$$

where $a = N_d / (N_d + N_a)$ is the oxidation-reduction factor dependent on the concentration of donors N_d and acceptors N_a . Photorefractive active donors and acceptors in LiNbO₃ are identified as Fe²⁺ and Fe³⁺ ions, respectively. E_D , E_{pv} , and E_q in Eq. (4) are the characteristic diffusion, photovoltaic, and saturation fields,

$$E_D = \frac{4\pi n_e k_B T \sin \left(\frac{\theta_s^{\text{in}}}{2} \right)}{\lambda e}, \quad E_{pv} = \frac{\beta I_p}{\sigma_{\text{ph}} + \sigma_d},$$

$$E_q = \frac{e\lambda N_{\text{eff}}}{4\pi\epsilon_{33}\epsilon_o \sin \left(\frac{\theta_s^{\text{in}}}{2} \right)}, \quad (5)$$

where T is the absolute temperature, k_B is the Boltzmann constant, e is the unit electric charge, β is the photovoltaic coefficient, I_p is the pump intensity, σ_{ph} and σ_d are the photo and dark conductivities, respectively, $\epsilon_{33}\epsilon_o$ is the static dielectric constant, and $N_{\text{eff}} = (N_d N_a / N_d + N_a)$ is the effective trap density. In the as-grown LiNbO₃, the photoconductivity is typically much higher than the dark conductivity, $\sigma_{\text{ph}} \gg \sigma_d$. In Eq. (4), the diffusion field in the $-c$ and $+c$ directions is characterized by the positive and negative signs, respectively.

At $E_q \gg E_{pv}, E_D$, which is the typical case for LiNbO₃, the coupling coefficient can be written [taking into account Eqs. (3) and (4)] as

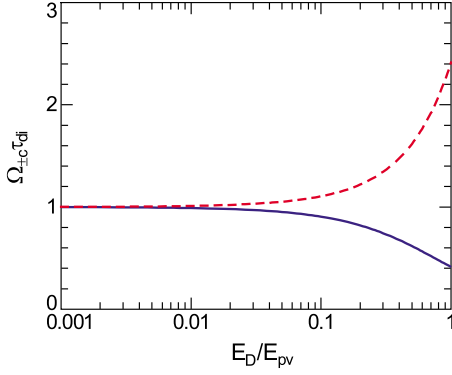


FIG. 2. (Color online) Dependence of frequency detuning $\Omega_{\pm c}\tau_{di}$ versus the field ratio E_D/E_{pv} . Solid and dashed lines correspond to the $-c$ and $+c$ branches.

$$\Gamma_{\pm c} = \frac{2\pi(\Omega_{\pm c}\tau_{di}E_{pv} \mp E_D)}{\lambda[1 + (\Omega_{\pm c}\tau_{di})^2]} \left[n_e^3 r_{33} \sqrt{\cos \theta_s^{\text{in}}} \cos\left(\frac{\theta_s^{\text{in}}}{2}\right) + n_e n_o^2 r_{51} \sqrt{\tan \theta_s^{\text{in}} \sin \theta_s^{\text{in}}} \sin\left(\frac{\theta_s^{\text{in}}}{2}\right) \right]. \quad (6)$$

It is different along and against the crystal polar axis because of the diffusion contribution. $\Gamma_{\pm c}$ represents the maxima of the dependence of the gain factor Γ versus the product $\Omega\tau_{di}$. In the general case, values $\Omega_{\pm c}\tau_{di}$ at which the function $\Gamma(\Omega\tau_{di})$ reaches the extremum are different in $\pm c$ directions [see, i.e., Fig. 6(a) in Ref. 2]. Therewith, the optimal frequency detuning $\Omega_{\pm c}$ is dependent on the ratio between the diffusion and photovoltaic field E_D/E_{pv} . Figure 2 shows the calculated dependence of $\Omega_{\pm c}\tau_{di}$ versus E_D/E_{pv} . The deviation of $\Omega_{\pm c}\tau_{di}$ from unity is very small for small E_D/E_{pv} , which is the case at small spatial frequencies: E_{pv} is independent on the scattering angle, but E_D is proportional to $\sin \theta_s^{\text{in}}$. Assuming $\Omega_{\pm c}\tau_{di}=1$, Eq. (6) can be reduced to

$$\Gamma_{\pm c} = \frac{\pi E_{pv} \left(1 \mp \frac{E_D}{E_{pv}}\right)}{\lambda} \left[n_e^3 r_{33} \sqrt{\cos \theta_s^{\text{in}}} \cos\left(\frac{\theta_s^{\text{in}}}{2}\right) + n_e n_o^2 r_{51} \sqrt{\tan \theta_s^{\text{in}} \sin \theta_s^{\text{in}}} \sin\left(\frac{\theta_s^{\text{in}}}{2}\right) \right]. \quad (7)$$

The photorefractive response in LiNbO₃ is rather slow, with the characteristic response time in the range of $\tau_{di} = 10^0 - 10^4$ s depending on the pump intensity. Therefore, for the case of $\Omega\tau_{di}$ not far from unity, the values of frequency detuning should be in the range of $\Omega = 10^0 - 10^{-4}$ Hz, respectively.

B. Initial scattering $I_{so}^{\Omega}(\theta_s)$

Since the low-frequency noise plays the key role in the scattering amplification properties of the initial scattering, it should also be described in terms of frequency detuning. In the assumption of a Lorentz dependence of the noise frequency spectrum, the preexponential factor I_{so}^{Ω} in Eq. (1) can be written as

$$I_{so}^{\Omega} = \frac{I_{so}}{1 + (\Omega_{\pm c}\tau_{di})^2}. \quad (8)$$

Here, we assume that only the components of the frequency spectrum corresponding to Ω_{-c} or Ω_{+c} are effectively amplified on gratings \mathbf{K} . All other components are suppressed and, therefore, can be neglected in our consideration. If $\Omega_{\pm c}\tau_{di} \neq 1$, then I_{so}^{Ω} is dependent on the field ratio E_D/E_{pv} . In the limiting case of $\Omega_{\pm c}\tau_{di} \approx 1$, Eq. (8) is reduced to $I_{so}^{\Omega} = I_{so}/2$.

C. Effective coupling length $l_{\text{eff}}(\theta_s)$

The effective coupling length l_{eff} in Eq. (1) is the distance between the points where the scattering component emerges from the scattering center and leaves the illuminated area. The analysis of the thickness dependence of PILS in photorefractive crystals shows that the major contribution to the scattering intensity I_s is from a thin region near the input face of the crystal.²⁰ Therefore, l_{eff} can be calculated as

$$l_{\text{eff}} = \frac{d}{\cos \theta_s^{\text{in}}}, \quad \text{for } \theta_s^{\text{in}} < \arctan\left(\frac{w_p}{2d}\right), \quad (9)$$

$$l_{\text{eff}} = \frac{w_p}{2 \sin \theta_s^{\text{in}}}, \quad \text{for } \theta_s^{\text{in}} \geq \arctan\left(\frac{w_p}{2d}\right), \quad (10)$$

where d is the crystal thickness and w_p is the width of the pump beam. A decrease of l_{eff} with increasing angle in Eq. (10) means that scattering components propagating at angles $\theta_s^{\text{in}} \geq \arctan\left(\frac{w_p}{2d}\right)$ leave the illuminated area that is already in the crystal volume. The larger the scattering angle is, the smaller the effective interaction length is.

D. Photoinduced light scattering method of crystal characterization

Equations (1)–(10) can be utilized to extract an important information about photorefractive properties of LiNbO₃ from the scattering intensity distribution. Among such parameters are the gain factor, photovoltaic, and diffusion fields.

The angular dependence of Γ can be retrieved from the initial $I_{so}^{\Omega}(\theta_s^{\text{in}})$ and stationary $I_s(\theta_s^{\text{in}})$ distributions of the scattering intensity measured in the plane of incidence. As follows from Eq. (1):

$$\Gamma(\theta_s^{\text{in}}) = \frac{1}{l_{\text{eff}}(\theta_s^{\text{in}})} \ln \frac{I_s(\theta_s^{\text{in}})}{I_{so}^{\Omega}(\theta_s^{\text{in}})}, \quad (11)$$

where $I_{so}^{\Omega}(\theta_s^{\text{in}})$ and $l_{\text{eff}}(\theta_s^{\text{in}})$ are taken from Eqs. (8)–(10), respectively. The photovoltaic $E_{pv}(\theta_s^{\text{in}})$ and diffusion $E_D(\theta_s^{\text{in}})$ fields can be retrieved from Eq. (6) as

$$E_{pv} = \frac{\frac{\lambda(\Gamma_{-c} + \Gamma_{+c})}{2\pi \left[n_e^3 r_{33} \sqrt{\cos \theta_s^{\text{in}} \cos\left(\frac{\theta_s^{\text{in}}}{2}\right)} + n_e n_o^2 r_{51} \sqrt{\tan \theta_s^{\text{in}} \sin \theta_s^{\text{in}} \sin\left(\frac{\theta_s^{\text{in}}}{2}\right)} \right]} - E_D \left(\frac{1}{1+(\Omega_{-c}\tau_{\text{di}})^2} - \frac{1}{1+(\Omega_{+c}\tau_{\text{di}})^2} \right)}{\frac{\Omega_{-c}\tau_{\text{di}}}{1+(\Omega_{-c}\tau_{\text{di}})^2} + \frac{\Omega_{+c}\tau_{\text{di}}}{1+(\Omega_{+c}\tau_{\text{di}})^2}}, \quad (12)$$

$$E_D = \frac{\frac{\lambda(\Gamma_{-c} - \Gamma_{+c})}{2\pi \left[n_e^3 r_{33} \sqrt{\cos \theta_s^{\text{in}} \cos\left(\frac{\theta_s^{\text{in}}}{2}\right)} + n_e n_o^2 r_{51} \sqrt{\tan \theta_s^{\text{in}} \sin \theta_s^{\text{in}} \sin\left(\frac{\theta_s^{\text{in}}}{2}\right)} \right]} - E_{pv} \left[\frac{\Omega_{-c}\tau_{\text{di}}}{1+(\Omega_{-c}\tau_{\text{di}})^2} - \frac{\Omega_{+c}\tau_{\text{di}}}{1+(\Omega_{+c}\tau_{\text{di}})^2} \right]}{\frac{1}{1+(\Omega_{-c}\tau_{\text{di}})^2} + \frac{1}{1+(\Omega_{+c}\tau_{\text{di}})^2}}, \quad (13)$$

where Γ_{-c} and Γ_{+c} are two branches of $\Gamma(\theta_s^{\text{in}})$ measured from Eq. (11). For $\Omega\tau_{\text{di}} \approx 1$, these expressions can be reduced to

$$E_{pv} = \frac{\lambda(\Gamma_{-c} + \Gamma_{+c})}{2\pi \left[n_e^3 r_{33} \sqrt{\cos \theta_s^{\text{in}} \cos\left(\frac{\theta_s^{\text{in}}}{2}\right)} + n_e n_o^2 r_{51} \sqrt{\tan \theta_s^{\text{in}} \sin \theta_s^{\text{in}} \sin\left(\frac{\theta_s^{\text{in}}}{2}\right)} \right]}, \quad (14)$$

$$E_D = \frac{\lambda(\Gamma_{-c} - \Gamma_{+c})}{2\pi \left[n_e^3 r_{33} \sqrt{\cos \theta_s^{\text{in}} \cos\left(\frac{\theta_s^{\text{in}}}{2}\right)} + n_e n_o^2 r_{51} \sqrt{\tan \theta_s^{\text{in}} \sin \theta_s^{\text{in}} \sin\left(\frac{\theta_s^{\text{in}}}{2}\right)} \right]}. \quad (15)$$

The scattering theory as well as the new PILS method of material characterization should be valid for doped and undoped LiNbO₃ crystals. Below, we will show how our approach can be applied to the most complicated case of undoped LiNbO₃, where the contributions of diffusion and photovoltaic effect to the charge transport are comparable, and the filed ratio E_D/E_{pv} strongly varies with the scattering angle θ_s .

It should be noted that the proposed approach can be applied to different photorefractive materials possessing diffusion and/or photovoltaic effect as major contributions to the electric charge transport, after proper modification of Eqs. (3)–(7), as well. The case of dominating diffusion charge transport ($E_{pv}=0$) and zero frequency detuning ($\Omega=0$) was already discussed at the example of SBN crystals.¹¹

III. EXPERIMENT SETUP AND RESULTS

The experiment is carried out with as-grown nominally undoped lithium niobate of the congruently melting composition. The residual concentration of iron, which is unavoidably present in the crystal due to the growing process, is $N_{\text{Fe}} = N_{\text{Fe}^{2+}} + N_{\text{Fe}^{3+}} \approx 1 \times 10^{17} \text{ cm}^{-3}$. The donor-to-acceptor ratio is $N_{\text{Fe}^{2+}}/N_{\text{Fe}^{3+}} \approx 0.1$, typical for an as-grown LiNbO₃. This allows to estimate the saturation field $E_q \geq 10 \text{ kV/cm}$, higher than the diffusion and photovoltaic fields induced in the transmission recording geometry. The LiNbO₃ sample of a thickness $d=3 \text{ mm}$ is cut normal to the b axis. The input and output surfaces of the dimension $a \times c = 6 \times 5 \text{ mm}^2$ are polished to optical quality. The c axis of the sample is oriented parallel to the table shown in Fig. 1. Crystal edges are short-circuited by conducting silver paste to avoid an accumulation of electric carriers.

The scattering is induced by the extraordinarily polarized pump beam from the continuous wave frequency-doubled Nd: yttrium aluminum garnet-laser ($\lambda=532 \text{ nm}$) with normal incidence to the crystal. The beam diameter is reduced to

a diameter of $w_{\text{FWHM}}=0.4 \text{ mm}$ after passing two lenses, $f1$ and $f2$. The optical absorption coefficient of the sample is $\alpha_{532 \text{ nm}}=6.2 \text{ m}^{-1}$.

The light distribution is measured by a Si-PIN photodiode (in Fig. 1) mounted on a computer-controlled motorized rotation stage. The photodiode runs around the sample in the plane of incidence in the angular range from -90° to $+90^\circ$. The angle $\theta_s=0^\circ$ defines the direction of the transmitted pump beam. The negative and positive angles correspond to the negative and positive directions of the c axis. The apex angle of the measured signal is limited to $\Delta\theta_s=0.4^\circ$ by the collimation system installed on the photodiode aperture to protect it from the background noise. In advance, the crystal and the photodiode are covered by a black box with a small opening for the pump beam.

First, the initial scattering distribution is measured at a probing intensity of $I_p=1 \text{ mW/cm}^2$ of the laser beam, which is insufficient to induce PILS during a single scan. The resulting intensity distribution $I_{\text{so}}(\theta_s^{\text{in}})$ recalculated to the angles in the crystal is shown by rectangles in Fig. 3. Then,

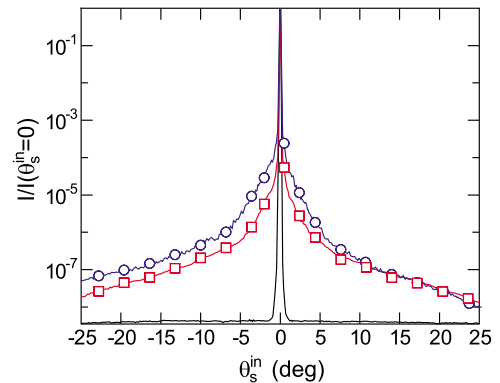


FIG. 3. (Color online) Angular intensity distribution of the initial scattering (rectangles), PILS pattern (circles), and pump beam (solid line), measured in the plane of incidence.

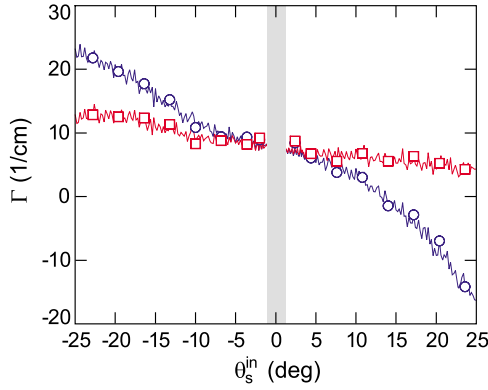


FIG. 4. (Color online) Angular dependence of the coupling coefficient retrieved from Eq. (11) in the assumption of $\Omega_{\pm c}\tau_{di}=1$ (circles) and $\Omega_{\pm c}\tau_{di}\neq 1$ (rectangles). In the central part influenced by the pump beam, the curves are dimmed by the gray bar.

the PILS pattern is induced at the pump intensity $I_p = 60 \text{ W/cm}^2$ for an exposure time of $t=60 \text{ min}$. After reaching the steady state, the intensity distribution is again scanned at a reduced intensity of $I_p=1 \text{ mW/cm}^2$. The corresponding intensity scan $I_s(\theta_s^{\text{in}})$ is shown by circles. The beam profile $I_p(\theta_s^{\text{in}})$, measured without the crystal, is shown by the solid line. All three curves are corrected to the “dark noise” measured at the closed opening of the black box and normalized to the maximum of the scattering scan. The comparison of the curves depicted in Fig. 3 shows that the central intensity peak of the $I_{so}(\theta_s^{\text{in}})$ and $I_s(\theta_s^{\text{in}})$ curves corresponds to the transmitted pump beam, which covers only a small angular interval $\Delta\theta_s^{\text{in}}=2.5^\circ$ in the center. It is obvious that the symmetric distribution of the initial scattering is changed to the asymmetric PILS profile. $I_s(\theta_s^{\text{in}})$ exceeds $I_{so}(\theta_s^{\text{in}})$ in the $-c$ direction and at small scattering angles in the $+c$ direction. At large positive angles, the PILS signal becomes smaller than the initial scattering. As it will be shown below, the angular behavior of the scattering can be explained in the frame of the discussed PILS model.

IV. DISCUSSION

According to the model above, we consider that the intensity profile $I_s(\theta_s^{\text{in}})$ is the coherent optical noise amplified due to the coupling of pump and scattering waves on photorefractive gratings at the presence of small frequency detuning and Eq. (1) can be applied. Therewith, the initial scattering profile $I_{so}^\Omega(\theta_s^{\text{in}})$ should be calculated from the experimental curve $I_{so}(\theta_s^{\text{in}})$ with the help of Eq. (8). Since the ratio E_D/E_{pv} is not known, the following analysis will be carried out in two steps: In the first approximation, we assume that the condition $E_{pv} \gg E_D$ is fulfilled and $\Omega\tau_{di}=1$, which is true at least for small K . Therefore, the initial scattering intensity in Eq. (1) is $I_{so}^\Omega(\theta_s^{\text{in}})=I_{so}(\theta_s^{\text{in}})/2$. Taking l_{eff} from Eqs. (9) and (10), the coupling coefficient is retrieved from Eq. (11). The resulting dependence of Γ versus the scattering angle θ_s^{in} is shown in Fig. 4 by circles. In the $-c$ direction, the coupling coefficient increases while in the $+c$ -direction, it decreases. This approximation gives us an extrapolation for the behav-

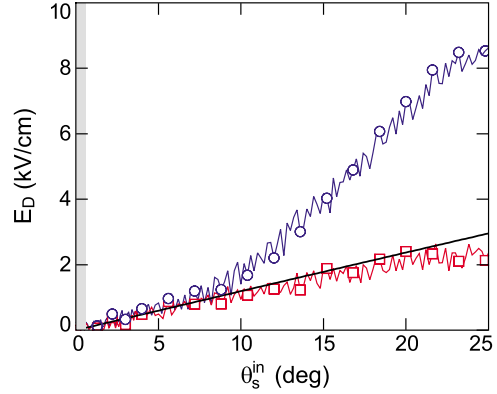


FIG. 5. (Color online) Angular dependence of the diffusion field E_D retrieved from Eqs. (15) (circles) and (13) (rectangles). Parts of curves influenced by the pump beam at small angles θ_s^{in} are dimmed by the gray bar.

ior of $E_D(\theta_s^{\text{in}})$ and $E_{pv}(\theta_s^{\text{in}})$. Angular dependencies of E_D and E_{pv} retrieved from Fig. 4 via Eqs. (14) and (15) are shown by circles in Figs. 5 and 6, respectively. The diffusion field calculated from Eq. (5) is shown in Fig. 5 by the solid line. A good agreement with Eq. (15) is observed at angles $\theta_s^{\text{in}} < 10^\circ$. For larger angles, a pronounced deviation from the theory to higher field values is obvious. Taking into account that the photovoltaic field is independent on the scattering angle, the fit of the experimental curve $E_{pv}(\theta_s^{\text{in}})$ to a constant in the angular range $\theta_s^{\text{in}} < 10^\circ$ gives $E_{pv}=3.7 \text{ kV cm}^{-1}$, as it is shown by the corresponding solid line in Fig. 6. For larger angles, the experimental curve decreases significantly.

The extrapolation of the theoretical lines to scattering angles $\theta_s^{\text{in}} \geq 10^\circ$ allows us to calculate the field ratio E_D/E_{pv} over the entire angular range. The result is shown in Fig. 7. The field ratio increases to $E_D/E_{pv} \approx 0.8$ at the largest angle but remains smaller than 0.3 for $\theta_s^{\text{in}} < 10^\circ$, where the best correlation between the experiment and the theory is found. The angular dependence of $\Omega_{\pm c}\tau_{di}$ calculated with the data presented in Figs. 2 and 7 is shown in Fig. 8. Over the entire angular interval, the frequency detuning $\Omega_{\pm c}\tau_{di}$ increases from 0.5 up to 2.1. These changes of $\Omega_{\pm c}\tau_{di}$ cause the de-

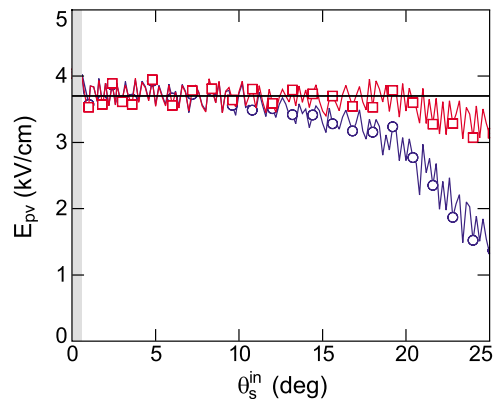


FIG. 6. (Color online) Angular dependence of the photovoltaic field E_{pv} retrieved from Eqs. (14) (circles) and (12) (rectangles). Parts of the curves influenced by the pump beam at small angles θ_s^{in} are dimmed by the gray bar.

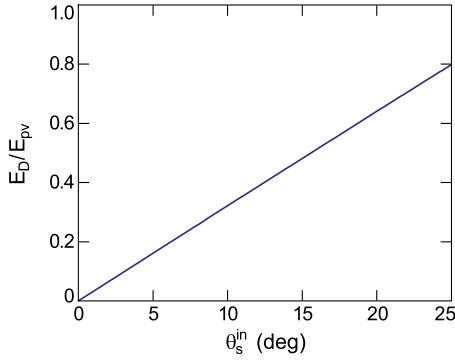


FIG. 7. (Color online) Dependence of the field ratio E_D/E_{pv} versus the scattering angle θ_s^{in} .

crease in the correction factor $I_{\text{so}}^{\Omega}/I_{\text{so}}$ [see Eq. (8)] from 0.8 to 0.2 for $-25^{\circ} \leq \theta_s^{\text{in}} \leq 25^{\circ}$.

Now, the corrected dependencies of crystal characteristics can be received in the second approximation. The substitution of $\Omega_{\pm c}(\theta_s^{\text{in}})\tau_{\text{di}}$ in Eq. (8) provides the modified dependence of the coupling coefficient calculated from Eq. (11) and shown in Fig. 4 by rectangles. The dependence has the same behavior as in the first approximation. However, it is reduced to the maximum value $\Gamma=14 \text{ cm}^{-1}$ and does not show negative values in the $+c$ direction because $E_D/E_{pv} < 1$. In its turn, the new dependencies $\Gamma(\theta_s^{\text{in}})$ and $\Omega_{\pm c}(\theta_s^{\text{in}})\tau_{\text{di}}$ applied to Eqs. (12) and (13) lead to considerably improved dependencies $E_{pv}(\theta_s^{\text{in}})$ and $E_D(\theta_s^{\text{in}})$, as shown by rectangles in Figs. 5 and 6, respectively. A satisfactory correlation with the corresponding theoretical curves is obvious almost for the entire angular interval. Deviations rising at $\theta_s^{\text{in}} > 20^{\circ}$ are, possibly, due to the increasing error in the detection of weak scattering signals. The determined photovoltaic field $E_{pv}=3.7 \text{ kV cm}^{-1}$ fits the general trend of the dependence of the photorefractive response in LiNbO_3 on the iron concentration. Furthermore, according to Ref. 21, the photovoltaic coefficient β_{33} decreases with the decreasing donor concentration $N_{\text{Fe}^{2+}}$, while the specific photoconductivity σ_{ph}/I_p is proportional to $N_{\text{Fe}^{2+}}/N_{\text{Fe}^{3+}}$. The extrapolation of the corresponding dependencies to the values $N_{\text{Fe}^{2+}}=1 \times 10^{16} \text{ cm}^{-3}$ and $N_{\text{Fe}^{2+}}/N_{\text{Fe}^{3+}}=0.1$, results in $E_{pv}=(0.5-5) \text{ kV cm}^{-1}$ for $\lambda=532 \text{ nm}$. Therefore, the PILS method gives rather reliable results for the photovoltaic field. At the same time, the diffusion field measured by the PILS method fits very well to the theory.

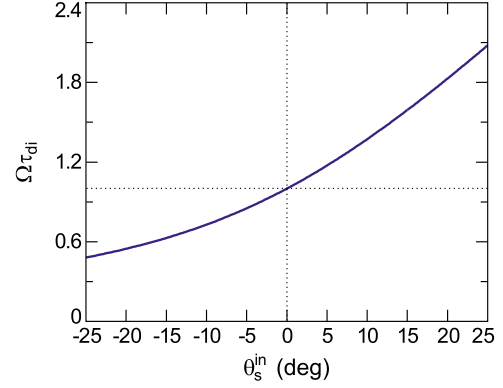


FIG. 8. (Color online) Dependence of frequency detuning $\Omega_{\pm c}\tau_{\text{di}}$ versus the scattering angle θ_s^{in} .

V. SUMMARY

The wide-angle polarization-isotropic scattering induced by a single pump beam of extraordinary polarization is studied in the undoped as-grown lithium niobate. The PILS model is considered, which explains the scattering as the result of 2WM on noisy photorefractive gratings at the presence of small frequency detuning. The model gives the qualitative, as well as quantitative, description of angular properties of the scattering if the dependence of frequency detuning on the ratio between the diffusion and photovoltaic fields is taken into account. Therewith, the new method of the determination of the angular dependence of the coupling coefficient Γ and of the photovoltaic E_{pv} and diffusion E_D fields from the comparative analysis of the initial and steady-state scattering distributions is proposed. It is shown that the experimental results are in good agreement with theoretical expectations for undoped lithium niobate. An ultimate simplicity together with very low requirements to the mechanical stability of the experimental setup make PILS-based methods very attractive and powerful tools for the nondestructive and contactless material characterization of photorefractive crystals. Results of these methods carried out with a doped LiNbO_3 crystals will be represented in our further publications.

ACKNOWLEDGMENTS

The work was supported by the Deutsche Forschungsgemeinschaft (DFG) within the framework of Projects No. GRK 695 and No. IM 37/2-2 and No. IM 37/5-1.

¹V. Voronov, I. Dorosh, Yu. Kuz'minov, and N. Tkachenko, *Sov. J. Quantum Electron.* **10**, 1346 (1980).

²M. Goukov, S. Odoulov, T. Woike, J. Imbrock, M. Imlau, E. Krätzig, C. Bäumer, and H. Hesse, *Phys. Rev. B* **65**, 195111 (2002).

³B. I. Sturman, S. G. Odoulov, and M. Yu. Goul'kov, *Phys. Rep.* **275**, 197 (1996).

⁴H. Rajbenbach, A. Delboulbe, and J. P. Huignard, *Opt. Lett.* **14**,

1275 (1989).

⁵J. Joseph, P. K. C. Pillai, and K. Sing, *Opt. Commun.* **80**, 84 (1990).

⁶J. Zhang, H. Wang, S. Yoshikado, and T. Aruga, *Opt. Lett.* **22**, 1612 (1997).

⁷J. Neumann, S. Mendricks, E. Krätzig, M. Goul'kov, and S. Odoulov, *Opt. Commun.* **146**, 220 (1998).

⁸T. Nakada, A. Okamoto, and K. Sato, *Opt. Commun.* **208**, 69

- (2002).
- ⁹U. van Olfen, R. A. Rupp, E. Kraetzig, and B. C. Grabmeier, *Ferroelectr., Lett. Sect.* **10**, 133 (1989).
- ¹⁰M. A. Ellabban, G. Mandula, M. Fally, R. A. Rupp, and L. Kovacs, *Phys. Lett.* **78**, 844 (2001).
- ¹¹M. Imlau, M. Goulkov, M. Fally, and Th. Woike, *Polar Oxides: Properties, Characterization and Imaging* (Wiley-VCH, Weinheim, 2005).
- ¹²M. Imlau, *Phys. Status Solidi A* **204**, 642 (2007).
- ¹³J. Feinberg, *J. Opt. Soc. Am.* **72**, 46 (1982).
- ¹⁴*Photorefractive Materials and Their Applications 3*, Springer Series in Optical Sciences Vol. 115, edited by P. Guenter and J. P. Huignard (Springer, New York, 2006).
- ¹⁵R. A. Rupp and F. W. Drees, *Appl. Phys. B: Photophys. Laser Chem.* **39**, 223 (1986).
- ¹⁶V. V. Lemanov and O. V. Kandidova, *Ferroelectrics* **95**, 15 (1989).
- ¹⁷A. Selinger, U. Voelker, V. Dieckmann, M. Imlau, and M. Goulkov, *Opt. Express* **15**, 4684 (2007).
- ¹⁸H. C. Pedersen, P. E. Andersen, and P. M. Johansen, *Opt. Lett.* **20**, 2475 (1995).
- ¹⁹H. Kogelnik, *Bell Syst. Tech. J.* **48**, 133 (1969).
- ²⁰M. Goulkov, K. Bastwoeste, S. Moeller, M. Imlau, and M. Woehlecke, *J. Phys.: Condens. Matter* **20**, 075225 (2008).
- ²¹R. Sommerfeldt, L. Holtmann, E. Kraetzig, and B. C. Grabmaier, *Phys. Status Solidi A* **106**, 89 (1988).